

Tightly-Coupled LiDAR-IMU-Wheel Odometry with Online Calibration of a Kinematic Model for Skid-Steering Robots

Taku Okawara¹, Kenji Koide², Shuji Oishi², Masashi Yokozuka², Atsuhiko Banno²,
Kentaro Uno¹, and Kazuya Yoshida¹

Abstract—Tunnels and long corridors are challenging environments for mobile robots because a LiDAR point cloud should degenerate in these environments. To tackle point cloud degeneration, this study presents a tightly-coupled LiDAR-IMU-wheel odometry algorithm with an online calibration for skid-steering robots. We propose a full linear wheel odometry factor, which not only serves as a motion constraint but also performs the online calibration of kinematic models for skid-steering robots. Despite the dynamically changing kinematic model (e.g., wheel radii changes caused by tire pressures) and terrain conditions, our method can address the model error via online calibration. Moreover, our method enables an accurate localization in cases of degenerated environments, such as long and straight corridors, by calibration while the LiDAR-IMU fusion sufficiently operates. Furthermore, we estimate the uncertainty (i.e., covariance matrix) of the wheel odometry online for creating a reasonable constraint. The proposed method is validated through three experiments. The first indoor experiment shows that the proposed method is robust in severe degeneracy cases (long corridors) and changes in the wheel radii. The second outdoor experiment demonstrates that our method accurately estimates the sensor trajectory despite being in rough outdoor terrain owing to online uncertainty estimation of wheel odometry. The third experiment shows the proposed online calibration enables robust odometry estimation in changing terrains.

I. INTRODUCTION

An accurate and robust odometry estimation is critical for autonomous robots to achieve reliable navigation and mapping in real-time. The state-of-the-art LiDAR odometry [1] and LiDAR IMU odometry [2], [3] can accurately estimate the robot pose owing to tight-coupling with LiDAR and IMU. However, these methods face challenges in environments where the LiDAR point clouds degenerate (e.g., long corridors and tunnels). Although IMU measurements can help in the short-term, IMU-based estimations accumulate drift and are corrupted by the long-term degeneration of LiDAR data. Conversely, wheel odometry can be a more reliable source of information in these LiDAR-degenerated situations because it provides consistent constraints of the robot movement that are independent of the environmental structure. Therefore, sensor fusion of the LiDAR, IMU,

*This work was supported in part by a project commissioned by the New Energy and Industrial Technology Development Organization (NEDO).

¹Taku Okawara, Kentaro Uno, and Kazuya Yoshida are with the Space Robotics Lab. in the Department of Aerospace Engineering, Graduate School of Engineering, Tohoku University, Sendai, Miyagi, Japan, okawara.taku.t3@dc.tohoku.ac.jp

²Kenji Koide, Shuji Oishi, Masashi Yokozuka, and Atsuhiko Banno are with the Department of Information Technology and Human Factors, the National Institute of Advanced Industrial Science and Technology, Tsukuba, Ibaraki, Japan

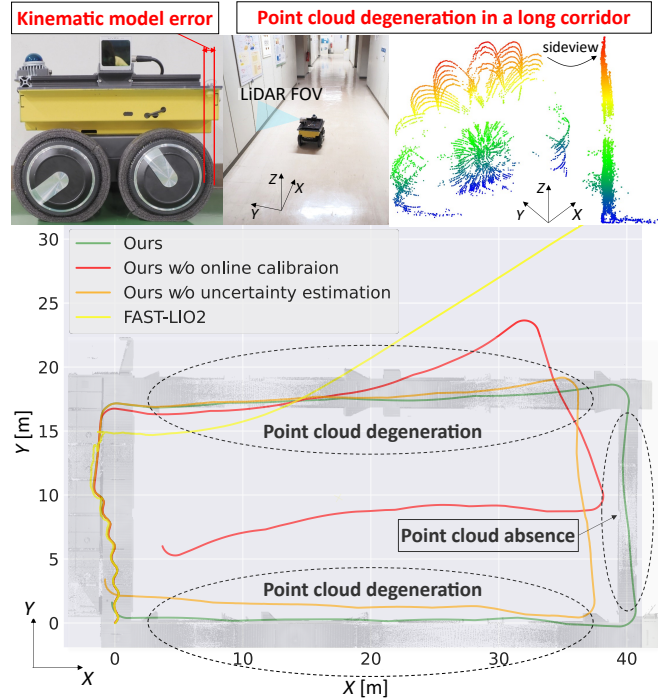


Fig. 1: A long corridor (top middle) or tunnel is representative of the challenging environment for mobile robots to localize and build maps due to point cloud degeneration. With the proposed method, even though a skid-steering robot with the kinematic model error (top left) experienced such degeneration of the point cloud (top right), the robot simultaneously accomplishes an accurate trajectory estimation (bottom) and online calibration of the kinematic parameters of the robot.

and wheel encoders can accomplish an accurate odometry estimation that is robust against the long-term degeneration of point clouds. Among wheel robots, skid-steering robots are widely used in various fields owing to their high road ability and mechanical simplicity. Skid-steering robots rotate by skidding their wheels based on different angular velocities of the left and right wheels, instead of using a steering mechanism. This mechanical simplicity makes the wheel odometry estimation more challenging compared to differential-drive robots because skid-steering robot's wheel odometry must consider terrain-dependent parameters (e.g., longitudinal and lateral slip ratio), the robot's center of mass, among others [4]. We consider that these parameters must be estimated online as the parameters dynamically change based on the terrain and wheel conditions.

In this study, we propose a tightly coupled-LiDAR IMU wheel odometry method with the online calibration of the kinematic parameters of wheel robots. This is formulated as a factor graph optimization problem. We especially tackle the online calibration for skid-steering robots as more challenging problems. As a general wheel odometry model, we used a full linear model that the velocity of the robot is assumed to be proportional to the angular velocity of the wheels. The online calibration of the full linear model can implicitly deal with unknown kinematic parameters and environments which is difficult to model rigorously. Therefore, we propose a *full linear wheel odometry factor* and jointly optimize the sensor trajectory and kinematic parameters online. Furthermore, we estimate the uncertainty (i.e., covariance matrix) of wheel odometry according to the roughness of the terrain and incorporate the uncertainty into the full linear wheel odometry factor. For example, for a flat terrain, the uncertainties along the height, roll, and pitch direction are estimated to be low, whereas for an uneven terrain, these uncertainties are large.

The main contributions of this study are three-fold:

- 1) We proposed a tightly coupled LiDAR-IMU-wheel odometry to resolve the severe degeneration of point clouds and the kinematic model errors of skid-steering robots. We jointly optimized the sensor trajectory and kinematic parameters, which depend on directly-non-observable phenomena or values (e.g., wheel slippage and kinematic model errors), using the full linear wheel odometry factor.
- 2) We explicitly estimated the covariance matrix for the full linear wheel odometry factor as a 3D motion. Experimental results validate that it can adapt the reliability of the full linear wheel odometry factor, resulting in accurate localization across environments with different ground surface conditions.
- 3) We publish a code of the full linear wheel odometry factor as an open source. <https://onl.la/Asn33BE>

II. RELATED WORK

A. Offline calibration for parameters of skid-steering robots

The wheel odometry computation of skid-steering robots involves parameters dependent on the environment and is complicated; thus, this problem has been addressed through offline calibration in many studies. For example, considering the extended differential drive [5], instantaneous centers of rotation (ICR) parameters were introduced to better model the motion of skid-steering robots by extending the ideal differential drive model. The radius of curvature (ROC)-based kinematic model [6] was experimentally derived based on the relationship between the ICR parameter and ROC of the robot motion. The full linear model [4] is a generic expression that describes the relationship between the velocity of the robot and the angular velocity of the wheels.

Furthermore, these methods have been evaluated in different environments, such as a flat plane and uneven terrain [7]. The results demonstrated that the full linear model is more accurate than the other methods owing to its flexibility according to the vehicle configurations and terrain conditions.

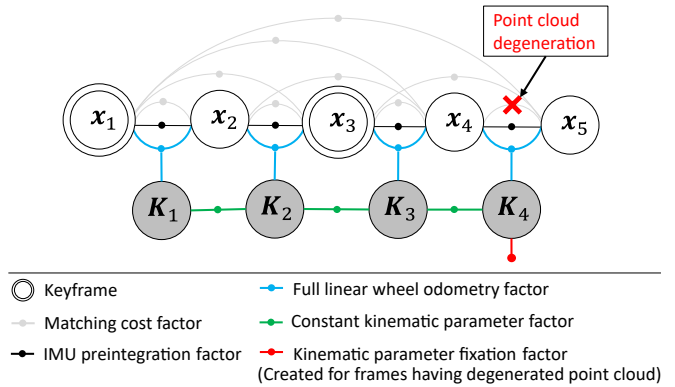


Fig. 2: Factor graph of the proposed method.

Notably, whereas these studies were conducted offline, the proposed method addresses online calibration.

B. Online calibration for wheel robots

In the case of wheel robots with a differential drive, some studies have conducted online calibration of kinematic parameters. Simultaneous Calibration, Localization, and Mapping [8], [9] were proposed to calibrate internal parameters (i.e., wheel radius and wheelbase) and simultaneously localize the robot pose. These methods applied a graph-based SLAM framework to the online calibration problem. In addition to the online calibration of the internal parameters, the extrinsic parameters between a robot frame and an IMU frame were incorporated into a Kalman filter-based visual-inertial odometry [10]. However, these approaches are based on the differential drive robots, assuming the ideal condition that wheel slippage does not occur.

Some works calculate the uncertainty of wheel odometry estimation by propagating an uncertainty of kinematic parameters and wheel encoder measurements [10], [11]. While these approaches calculate only the uncertainty of 2D motion for wheel odometry in principle, we estimate the uncertainty in 3D by incorporating LiDAR and IMU measurements.

The most relevant studies are [12], [13], which conducted vision-based online calibration of kinematic models for skid-steering robots. These methods demonstrated that a fusing of vision and IMU, and ICR-based wheel odometry [5] with online calibration enables a more accurate estimation than visual IMU fusions. However, while these approaches were not validated in featureless environments, the proposed method was demonstrated to perform highly accurate odometry estimation in severe featureless environments by handling degeneracy of the LiDAR point cloud. Furthermore, these methods do not explicitly estimate the uncertainty of the wheel odometry model in 3D.

III. METHODOLOGY

A. System Overview

An overview of the proposed odometry estimation based on the online calibration of the kinematic model for skid-steering robots is described. The state to be estimated is

defined as follows:

$$\mathbf{X}_t = [\mathbf{x}_t, \mathbf{K}_t], \quad (1)$$

$$\mathbf{x}_t = [\mathbf{T}_t, \mathbf{v}_t, \mathbf{b}_t], \quad (2)$$

where \mathbf{x}_t is a frame state, $\mathbf{T}_t = [\mathbf{R}_t | \mathbf{t}_t] \in SE(3)$ is the IMU pose, $\mathbf{v}_t \in \mathbb{R}^3$ is the velocity, $\mathbf{b}_t = [\mathbf{b}_t^a, \mathbf{b}_t^\omega] \in \mathbb{R}^6$ is the bias of the IMU acceleration \mathbf{a}_t and the angular velocity $\boldsymbol{\omega}_t$. \mathbf{K}_t indicates the kinematic parameters of the skid-steering robots. LiDAR, IMU, and wheel encoders were used as measurement sources to construct the factor graph, as shown in Fig. 2. Keyframes are a set of frames that have a moderate overlap and help reduce the estimation drift. For simplicity, LiDAR point clouds and velocity calculated by the wheel encoders are transformed into the IMU frame as if they are in the same frame. Details regarding each factor will be explained in the following subsections.

We assume that \mathbf{K}_t is optimized online along with the sensor states in feature-rich environments before entering environments where LiDAR point clouds can degenerate. Once the kinematic model converges to a proper solution, it helps maintain a well-constrained estimation and enables an accurate odometry estimation even in such environments.

B. Matching Cost Factor

We use the voxelized GICP (VGICP)-based point cloud matching cost factor to constrain many frames in real-time with GPU acceleration [14]. In VGICP, each input point $\mathbf{p}_k \in \mathcal{P}_i$ is treated as a Gaussian distribution $\mathbf{p}_k = (\boldsymbol{\mu}_k, \mathbf{C}_k)$, where $\boldsymbol{\mu}_k$ and \mathbf{C}_k are the mean and covariance matrix of the neighbors of \mathbf{p}_k , respectively. Target points \mathcal{P}_j are discretized by voxelization, and each voxel stores the average of the means and covariance matrices in that voxel. This voxelization enables a quick nearest neighbor search through spatial hashing [15]. The matching cost factor [16] constrains \mathbf{T}_i and \mathbf{T}_j , such that point cloud \mathcal{P}_i is aligned to the voxelized \mathcal{P}_j . In conclusion, the matching cost e_{ij}^M is defined as follows:

$$e_{ij}^M(\mathcal{P}_i, \mathcal{P}_j, \mathbf{T}_i, \mathbf{T}_j) = \sum_{\mathbf{p}_k \in \mathcal{P}_i} e_{ij}^{\text{D2D}}(\mathbf{p}_k, \mathbf{T}_i^{-1} \mathbf{T}_j), \quad (3)$$

$$e_{ij}^{\text{D2D}}(\mathbf{p}_k, \mathbf{T}_{ij}) = \mathbf{d}_k^\top (\mathbf{C}'_k + \mathbf{T}_{ij} \mathbf{C}_k \mathbf{T}_{ij}^\top)^{-1} \mathbf{d}_k, \quad (4)$$

where e_{ij}^{D2D} is the distribution-to-distribution distance between an input point \mathbf{p}_k and the corresponding voxel $\mathbf{p}'_k = (\boldsymbol{\mu}'_k, \mathbf{C}'_k)$, and $\mathbf{d}_k = \boldsymbol{\mu}'_k - \mathbf{T}_{ij} \boldsymbol{\mu}_k$ is the residual between $\boldsymbol{\mu}_k$ and $\boldsymbol{\mu}'_k$. Further details can be found in [17] (point cloud processing, strategy of keyframe selection, etc.). Each frame is constrained by matching cost factors with the last N (e.g., 3) frames and keyframes, as shown in Fig. 2.

C. IMU Preintegration Factor

The IMU preintegration factor constrains the relative pose and velocity between two consecutive frames by integrating multiple IMU measurements (\mathbf{a}_i and $\boldsymbol{\omega}_i$), as shown in Fig. 2. This technique is vital for efficiently fusing high-frequency IMU measurements and low-frequency sensor measurements (e.g., point clouds). The IMU measurements update the

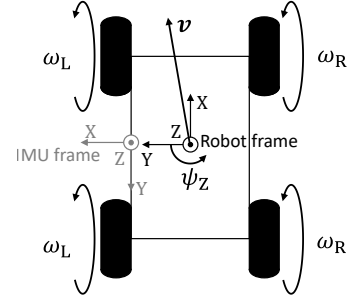


Fig. 3: Diagram for kinematics of skid-steering robots. Note that the result of wheel odometry described in the robot frame is finally transformed into the IMU frame.

sensor state in a time interval Δt (i.e., a frequency of IMU measurements) as follows:

$$\mathbf{R}_{t+\Delta t} = \mathbf{R}_t \exp((\boldsymbol{\omega}_t - \mathbf{b}_t^\omega - \boldsymbol{\eta}_t^\omega) \Delta t), \quad (5)$$

$$\mathbf{v}_{t+\Delta t} = \mathbf{v}_t + \mathbf{g} \Delta t + \mathbf{R}_t (\mathbf{a}_t - \mathbf{b}_t^a - \boldsymbol{\eta}_t^a) \Delta t, \quad (6)$$

$$\mathbf{t}_{t+\Delta t} = \mathbf{t}_t + \mathbf{v}_t \Delta t + \frac{1}{2} \mathbf{g} \Delta t^2 + \frac{1}{2} \mathbf{R}_t (\mathbf{a}_t - \mathbf{b}_t^a - \boldsymbol{\eta}_t^a) \Delta t^2, \quad (7)$$

where \mathbf{g} is the gravity vector and $\boldsymbol{\eta}_t^a$ and $\boldsymbol{\eta}_t^\omega$ represent the white noise of the IMU measurement. We can calculate a relative sensor motion $\Delta \mathbf{R}_{ij}$, $\Delta \mathbf{v}_{ij}$, and $\Delta \mathbf{t}_{ij}$ by integrating $\Delta \mathbf{R}_{t+\Delta t}$, $\Delta \mathbf{v}_{t+\Delta t}$, and $\Delta \mathbf{t}_{t+\Delta t}$ between time steps i and j , respectively. The error e_{ij}^{IMU} between \mathbf{x}_i and \mathbf{x}_j is finally defined as follows:

$$e_{ij}^{\text{IMU}}(\mathbf{x}_i, \mathbf{x}_j) = \left\| \log \left(\Delta \mathbf{R}_{ij}^T \mathbf{R}_i^T \mathbf{R}_j \right) \right\|^2 + \left\| \Delta \mathbf{t}_{ij} - \mathbf{R}_i^T \left(\mathbf{t}_j - \mathbf{t}_i - \mathbf{v} \Delta t_{ij} - \frac{1}{2} \mathbf{g} \Delta t_{ij}^2 \right) \right\|^2 + \left\| \Delta \mathbf{v}_{ij} - \mathbf{R}_i^T (\mathbf{v}_j - \mathbf{v}_i - \mathbf{g} \Delta t_{ij}) \right\|^2. \quad (8)$$

Further details can be found in [18]. The IMU preintegration factor makes an estimation robust to rapid motions and degeneracy of point clouds in a short time. In addition, this factor reduces the estimation drift in four DOFs [19].

D. Full Linear Wheel Odometry Factor

To describe the robot motion using wheel encoder values (i.e., wheel odometry estimation), we employed the full linear odometry model [4]. Compared to other parametric models (e.g., [5], [6]), the full linear model exhibits effective characteristics accounting for the asymmetry of the structure of the robot, mechanical modeling errors, and ground surface changes that are difficult to explicitly model.

Wheel odometry provides relative transformation and velocity based on kinematic and terrain-dependent parameters, and measurements of wheel encoders. For skid-steering robots, the velocity $[\mathbf{v} \ \psi_z]^\top$ is calculated as follows:

$$\begin{bmatrix} \mathbf{v} \\ \psi_z \end{bmatrix} = \mathbf{J} \begin{bmatrix} \omega_L \\ \omega_R \end{bmatrix}, \quad (9)$$

where $\mathbf{v} = [v_x \ v_y]^\top$ is the 2D translational velocity, ψ_z is the angular velocity around the z-axis of the robot frame, and $\boldsymbol{\omega} = [\omega_L \ \omega_R]^\top$ is the angular velocity of the left and

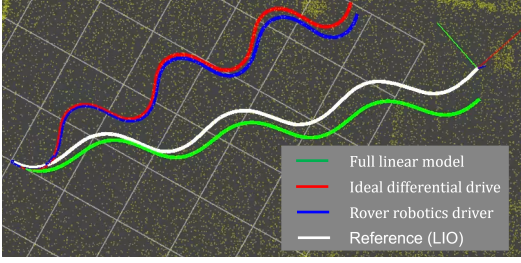


Fig. 4: Accuracy validation of the full linear model.

right wheels, as shown in Fig. 3. \mathbf{J} is a 3×2 matrix that describes the relationship between $[\mathbf{v} \ \psi_z]^\top$ and $\boldsymbol{\omega}$ depending on the following kinematic and terrain parameters:

$$\mathbf{J} = \begin{bmatrix} J_{11} & J_{12} \\ J_{21} & J_{22} \\ J_{31} & J_{32} \end{bmatrix}. \quad (10)$$

Here, \mathbf{J} is expressed with the parameter vector \mathbf{K} as follows:

$$\mathbf{K} = [J_{11} \ J_{12} \ J_{21} \ J_{22} \ J_{31} \ J_{32}]^\top. \quad (11)$$

We regard \mathbf{K} as a time variant value \mathbf{K}_i as stated in Eq. 1. The full linear wheel odometry factor is a motion constraint depending not only on the robot poses but also \mathbf{K}_i . Therefore, \mathbf{K}_i is calibrated such that the factor graph is optimized. The full linear wheel odometry factor is created between consecutive frame states (e.g., \mathbf{x}_i and \mathbf{x}_j) and the corresponding kinematic parameter (e.g., \mathbf{K}_i), as shown in Fig. 2. We then describe an initial value \mathbf{K}_0 for factor graph optimization. We use the kinematic parameters of an ideal differential drive model, which does not consider wheel slippage and lateral motion. Hence, \mathbf{K}_0 is set as follows:

$$\mathbf{K}_0 = [R/2 \ R/2 \ 0 \ 0 \ -R/B \ R/B]^\top, \quad (12)$$

where R and B are nominal values indicating the wheel radius and wheelbase of the robot, respectively.

The displacement $\Delta \mathbf{o}_{ij} \in se(2)$ is calculated by integrating $[\omega_L \ \omega_R]^\top$ between the time steps i and j as follows:

$$\Delta \mathbf{o}_{ij} = \mathbf{J}_i \begin{bmatrix} \Delta \theta_{L,ij} \\ \Delta \theta_{R,ij} \end{bmatrix}, \quad (13)$$

where $\Delta \theta_{L,ij} = \int_i^j \omega_L dt$, $\Delta \theta_{R,ij} = \int_i^j \omega_R dt$ are the angular displacements of the left and right wheels, respectively. We then extend $\Delta \mathbf{o}_{ij} \in se(2)$ into $\Delta \mathbf{O}_{ij} \in se(3)$ by setting the translational z and rotational x, y elements to zero. Here, $\Delta \mathbf{O}_{ij}$ is the robot motion described in the robot frame; this motion is treated as the IMU motion $\Delta \mathbf{O}_{ij}$ in our implementation. Therefore, $\Delta \mathbf{O}_{ij}$ is transformed into $\Delta \mathbf{O}_{ij}^W$. The wheel odometry error \mathbf{r}_{ij}^W is defined as follows:

$$\mathbf{r}_{ij}^W = \log(\mathbf{T}_i^{-1} \mathbf{T}_j \exp(\Delta \mathbf{O}_{ij}^{-1})). \quad (14)$$

Consequently, the wheel odometry cost e_{ij}^W is defined as follows:

$$e_{ij}^W = \mathbf{r}_{ij}^{W\top} \mathbf{C}_{ij}^{W-1} \mathbf{r}_{ij}^W, \quad (15)$$

where \mathbf{C}_{ij}^{W-1} is the covariance matrix of wheel odometry that is derived as indicated in III-G.

Fig 4 demonstrates an example of the wheel odometry estimation results using the online-calibrated full linear model in comparison to using the conventional ideal differential drive model. For reference, the odometry output of the rover robotics official driver and LiDAR-IMU odometry are also shown. The ideal differential model uses the values of \mathbf{K}_0 . The calibrated full linear model demonstrates a trajectory similar to that of the LiDAR-IMU odometry, and this result shows that this model is the most accurate among these wheel odometry models. In addition, we can infer that the official driver is likely computing the wheel odometry similar to that of the ideal differential model.

E. Constant Kinematic Parameter Factor

A constant kinematic parameter factor constrains the consecutive kinematic parameters \mathbf{K}_i based on a zero-mean Gaussian noise as shown in Fig. 2. In the case of approaches related to the IMU preintegration factor, this technique is widely used for modeling random walk bias evolution. We use this factor for adapting the kinematic parameters to a change in terrain conditions (e.g., a transition from an outdoor to an indoor environment). In our implementation, we set all diagonal elements of a covariance matrix of this factor to 10^{-10} .

F. Kinematic Parameter Fixation Factor

The full linear wheel odometry factor also performs the online calibration for \mathbf{K}_i in addition to serving as a motion constraint. Therefore, the online calibration can be unstable if point clouds degenerate. To avoid this situation, we create a kinematic parameter fixation factor for \mathbf{K}_i as shown in Fig. 2 when the point cloud degeneration is detected on the corresponding frames. We detect point cloud degeneration by considering the linearized system after the factor graph optimization. This process consists of the following two steps: 1) the Hessian matrix of a matching cost factor between the latest and last frames is calculated, and 2) if the minimum eigenvalue of the Hessian matrix is smaller than a threshold (the Hessian matrix is not positive definite), the latest frame is detected as degeneracy. If the current point cloud \mathcal{P}_j is determined as degeneracy, the kinematic parameter fixation factor for \mathbf{K}_i is added such that \mathbf{K}_i becomes those retained just before degeneracy occurs to avoid corrupting the optimization. We set all diagonal elements of a covariance matrix of the kinematic parameter fixation factor to 10^{-10} in our implementation. We also create similar factors for the IMU bias to make optimization stable.

G. Uncertainty Estimation for Wheel Odometry

We regard the uncertainty of wheel odometry as a covariance matrix \mathbf{C}_{ij}^{W-1} . Each component of the wheel odometry residual $(r_{ij,x}^W, r_{ij,y}^W, r_{ij,z}^W, r_{ij,roll}^W, r_{ij,pitch}^W, r_{ij,yaw}^W)$ is assumed to be proportional to the wheel angular displacement $\Delta \theta_{ij}$:

$$r_{ij,x}^W = \Delta \theta_{ij} a_{j,x}, \quad (16)$$

$$\Delta \theta_{ij} = |\Delta \theta_{L,ij}| + |\Delta \theta_{R,ij}|, \quad (17)$$

where $a_{j,x}$ is a positive propositional coefficient for the translational x . We estimate $a_{j,x}$ based on a one-dimensional Kalman filter online. A constant mean model is also assumed for the state transition of the Kalman filter. Therefore, the state and measurement equations are defined as follows:

$$a_{j,x} = a_{i,x} + q_i, \quad (18)$$

$$r_{ij,x}^W = \Delta\theta_{ij}a_{j,x} + s_i, \quad (19)$$

where q_i and s_i indicate the white noise following the constant process noise Q and observation noise S , respectively. According to these equations, $a_{j,x}$ is iteratively updated by the following steps:

$$k_j = \frac{\Delta\theta_{ij}(P_i + Q)}{\Delta\theta_{ij}^2(P_i + Q) + S}, \quad (20)$$

$$a_{j,x} = a_{i,x} + k_j(r_{ij,x}^W - \Delta\theta_{ij}a_{i,x}), \quad (21)$$

$$P_j = (1 - \Delta\theta_{ij}k_j)(P_i + Q), \quad (22)$$

where k_j is the Kalman gain and P_j is the variance of $a_{j,x}$. In our implementation, the initial variance was $P_0 = 1000$, the initial state was $a_{0,x} = 0$, and $Q = 10^{-11}$, $S = 10^{-3}$. The variance of wheel odometry $\sigma_{x,ij}^2$ is calculated as follows:

$$\sigma_{x,ij}^2 = (a_{j,x}\Delta\theta_{ij})^2. \quad (23)$$

Other than the translational x , the variances are computed similarly. We assume that each component of wheel odometry is independent; thus, $C_{ij}^{W^{-1}}$ contains values only in its diagonal components. $(\sigma_{x,ij}^2, \sigma_{y,ij}^2, \sigma_{z,ij}^2, \sigma_{roll,ij}^2, \sigma_{pitch,ij}^2, \sigma_{yaw,ij}^2)$ are set to the corresponding diagonal component in $C_{ij}^{W^{-1}}$. A constant covariance matrix (e.g. translational elements, rotational elements are set to $3.6 \times 10^{-5} \text{ m}^2$, $2.3 \times 10^{-5} \text{ rad}^2$ respectively) is used in the first few steps where the observation is insufficient. Specifically, $C_{ij}^{W^{-1}}$ is estimated when variances of kinematic parameters K_i being results of the optimization converge to a value.

IV. EXPERIMENTAL RESULTS

A. Experimental Setup

The proposed factor graph was implemented using GT-SAM and the iSAM2 [20] optimizer was used to incrementally optimize the factor graph. Rover mini (Rover Robotics) was used as a testbed. We recorded the point cloud and IMU data using a narrow FOV LiDAR (Livox AVIA) along with the wheel encoder values. The narrow FOV LiDAR was used for imitating point cloud degeneration in severe environments, such as tunnels. Point clouds, IMU measurements, and the wheel angular velocities were recorded at 10, 200, and 60 Hz, respectively. A velocity command was given to a robot controller for the initial approximately 20 seconds of all the experiments, such that the robot followed a sine curve trajectory for the initial calibration of all elements of the kinematics parameters K_i . We assume that K_i is calibrated online in feature-rich environments before entering environments where LiDAR point clouds can degenerate, and thus a start location of the robot for all experiments was in a feature-rich environment.

TABLE I: Ratio of frames encountering degeneracy and absence of the point clouds.

	Point cloud degeneracy	Point cloud absence
Ratio of frames	53 % (1601/3029)	15 % (447/3029)

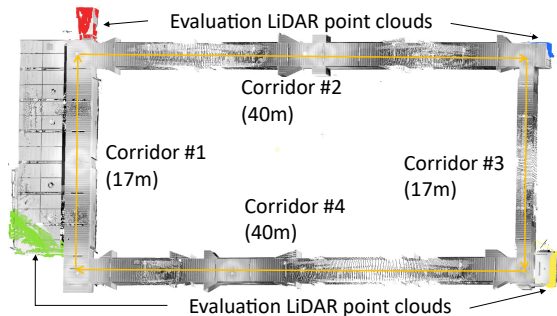


Fig. 5: The indoor environment including long corridors. The robot traveled about 120 m, from the Corridor #1 to #4. *Evaluation LiDAR point clouds* are only used for obtaining the ground truth of the relative sensor position at each corner.

The proposed method was compared with FAST-LIO2 [3], which is a state-of-the-art LiDAR-IMU odometry method based on tightly coupled point cloud and IMU constraints. In addition, the proposed method (Ours) was also compared with the following methods as ablation studies.

- *Ours w/o online calibration*: Constant kinematics parameters K_0 derived from the ideal differential drive model (Eq. 12) were set for constructing the wheel odometry-based constraints without online calibration. This ideal differential drive model provides nearly the same odometry estimation results as that of the official rover robotics driver (Fig 4); thus, it was considered a reasonable choice.
- *Ours w/o uncertainty estimation*: Constant uncertainties (i.e. covariance matrix) are always set to each full linear wheel odometry factor.

B. Indoor Environment

The objective of this experiment was to demonstrate that the full linear wheel odometry factor significantly improves the robustness to point cloud degeneracy and kinematic model errors. As shown in Fig. 5, the indoor environment consists of long corridors. Table I summarizes the number of frames where the point cloud data was 1) degenerated, and 2) unavailable (the number of points was lower than 100). Notably, the narrow FOV LiDAR was always pointed at the walls of the corridors in this experiment; thus, the observed point clouds were mostly degenerated (53 % of all frames). Because the LiDAR cannot observe points closer than the minimum observation range (1 m), the point cloud measurements became completely unavailable when the sensor approached the wall (15 % of all frames).

Furthermore, we modified the wheels by attaching Styrofoam belts to increase the radius of all the wheels of the robot by 25 %. We used K_0 defined by Eq. 12 as the initial guess to validate the effectiveness of the online calibration.

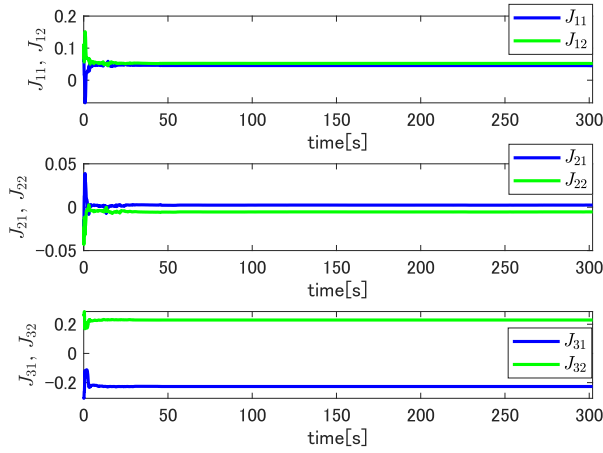


Fig. 6: Time histories of the kinematic parameters of the skid-steering robot K_i . K_i is few changed after the first 30 seconds because the almost point clouds were degenerated.

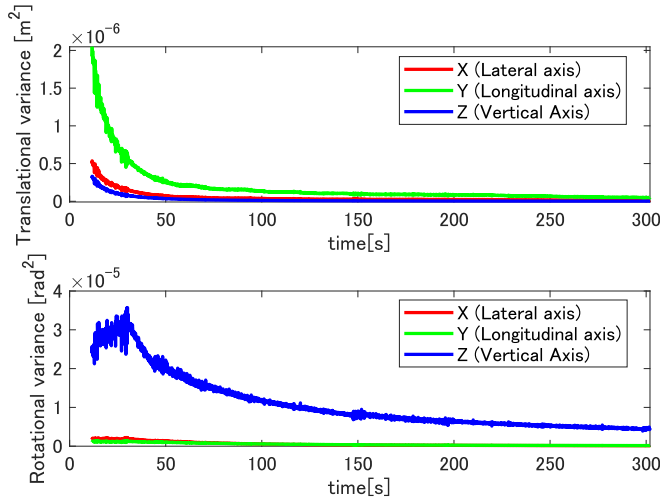


Fig. 7: Time histories of the diagonal elements of C_{ij}^{W-1} in the indoor environment. Note that C_{ij}^{W-1} is described with respect to the IMU frame as seen in Fig. 3.

Ground truth sensor poses were obtained at the corners by manually aligning the *evaluation LiDAR point clouds* into a prior map (Fig. 5). The prior map was obtained by a 3D laser scanner, Focus3D X330 (FARO).

Table II presents a quantitative analysis of the relative position errors of all methods for Corridor #1 to #4. Accuracy of the proposed method outperforms all other approaches, as shown in Fig. 1, Table II. We can see that both the online kinematics parameter calibration and the uncertainty estimation contributed to the trajectory estimation accuracy. Although Corridor #3 includes intervals where no point cloud data is obtained owing to the narrow width of the corridor, odometry estimation remains accurate. Therefore, this result validates that the proposed method is robust not only to point cloud degeneracy but also to absence of points.

Fig. 6 demonstrates that the kinematic parameters K_i rapidly converge to reasonable values even though the parameters were initialized with clearly improper values. J_{11} is almost the same as J_{12} . In addition, J_{21} and J_{31} exhibit

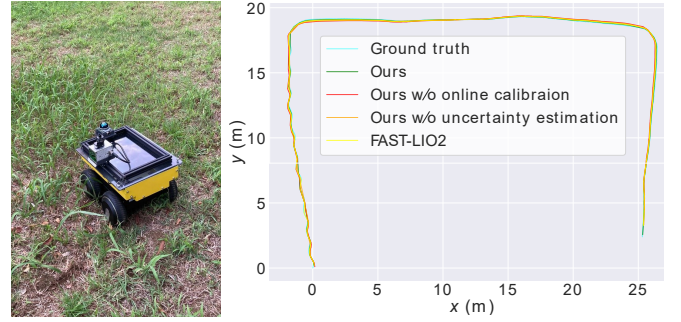


Fig. 8: Outdoor environment and trajectory estimation result.

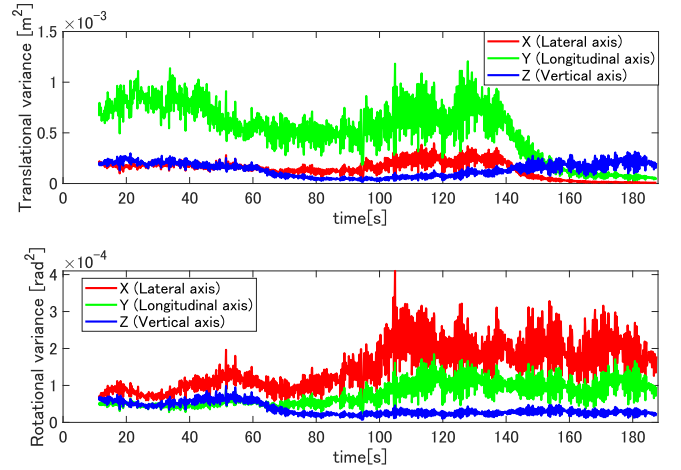


Fig. 9: Time histories of the diagonal elements of C_{ij}^{W-1} in an outdoor environment; the overall components are larger compared to those indoors (Fig. 7).

approximate symmetry with respect to J_{22} and J_{32} , respectively, thus the result of online calibration is reasonable. Note that K_i is few changed after the first 30 seconds because many *kinematic parameter fixation factors* were created because this indoor environment was the condition almost point clouds degenerate.

Fig. 7 is the result of the online estimation of the wheel odometry uncertainties C_{ij}^{W-1} . The translational y direction (longitudinal axis) and the yaw direction are larger than the other corresponding elements because the robot was moving on a flat surface.

C. Outdoor Environment

The uncertainty estimation of the wheel odometry is important for managing 3D motion fluctuations on uneven terrains. To demonstrate the effectiveness and validity of the online uncertainty estimations for such 3D motion fluctuation, the *Ours w/o uncertainty estimation* case is set up with a constant covariance matrix which is obtained by the final values of C_{ij}^{W-1} estimated in Fig. 7 (these values were validated to properly perform in the flat floor by the IV-B result). We obtained the ground truth of the sensor trajectory by using a total station, Trimble S9.

Fig. 8 shows the outdoor environment (grass) and the trajectory comparison. Owing to the feature-rich environment, all trajectories are estimated properly. Table III indicates

TABLE II: Comparison of relative position errors from Corridor #1 to #4 (average and standard deviation of 8 experiments).

	Ours	Ours w/o online calibration	Ours w/o uncertainty estimation	FAST-LIO2
#1 (17 m)	0.539 ± 0.144 m	1.176 ± 0.271 m	0.565 ± 0.143 m	2.283 ± 0.558 m
#2 (40 m)	2.188 ± 0.521 m	8.215 ± 0.600 m	4.900 ± 0.363 m	Error >10 m
#3 (40 m)	0.770 ± 0.110 m	4.907 ± 0.361 m	1.118 ± 0.120 m	Error >10 m
#4 (17 m)	1.467 ± 0.331 m	9.118 ± 1.643 m	4.710 ± 0.454 m	Error >10 m

TABLE III: ATE comparison in the outdoor environment. The robot traveled about 64 m.

Methods	ATE [m]
Ours	0.049 ± 0.017
Ours w/o online calibration	0.114 ± 0.041
Ours w/o uncertainty estimation	0.092 ± 0.034
FAST-LIO2	0.068 ± 0.024

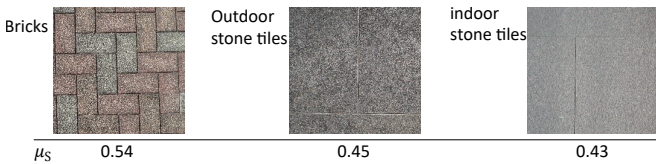


Fig. 10: Transition of terrain condition in the third experiment; left: bricks, center: outdoor stone tiles, right: indoor stone tiles. As a reference of the ground roughness, we measured each condition’s static friction coefficient μ_s .

an absolute trajectory error (ATE) [21], and this result shows that the proposed method is the most accurate in all approaches owing to the online calibration and online uncertainty estimation. Fig. 9 demonstrates the results of the wheel odometry uncertainty estimation. The overall components are larger compared to the corresponding values for the indoor flat floor (Fig. 7). The estimated variances in the roll and pitch directions are particularly large in this environment owing to the uneven ground, thus the result of the online uncertainty estimation is reasonable. Including the proper uncertainty estimation resulted in twice the accuracy compared to the condition where it was not included.

D. Transition from Outdoor to Indoor Environment

The objective of this experiment was to demonstrate that the proposed online calibration enables robust odometry estimation in changing terrain conditions. In this experiment, the robot transited the following terrain conditions: 1) bricks, 2) outdoor stone tiles, and 3) indoor stone tiles, as shown in Fig. 10. The environment included three point cloud degeneration spots for validating whether kinematic parameter

TABLE IV: ATE comparison in the case of transition from bricks to outdoor stone tiles, indoor stone tiles. The robot traveled about 144 m.

Methods	ATE [m]
Ours	0.794 ± 0.568
Ours w/o online calibration	3.118 ± 2.616
Ours w/o uncertainty estimation	0.997 ± 1.123
FAST-LIO2	Error >10 m

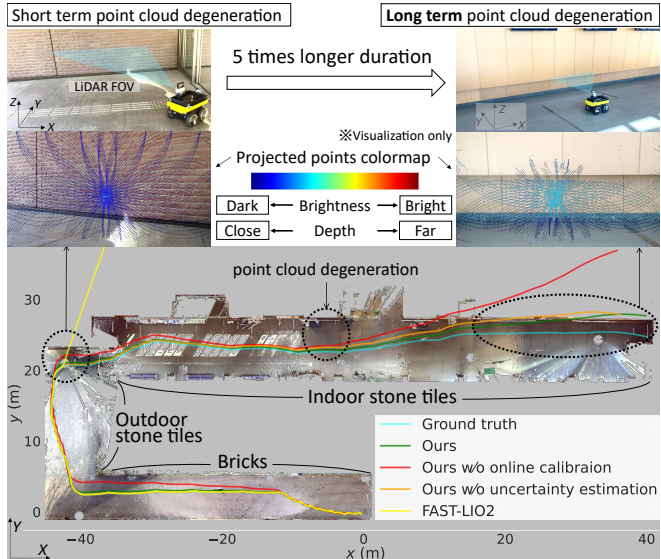


Fig. 11: Trajectory estimation results in the case of transition from bricks to outdoor stone tiles, indoor stone tiles. The upper images are perspective views, and subjective views from the LiDAR. The subjective views include points projected point clouds of the LiDAR for visualization only. The points are colored by colormap (JET) based on the depth and brightness of each point, and thus spreading the same colored points in the same planes (e.g., wall, floor) should mean the LiDAR point cloud is degenerated.

K_i is calibrated properly. In this experiment, point clouds of an omnidirectional FOV LiDAR (Livox MID-360) and its IMU data are recorded in addition to the narrow FOV LiDAR for estimating a reference trajectory as ground truth. We manually aligned point clouds of the omnidirectional FOV LiDAR with a prior map (constructed by the same 3D laser scanner as used in IV-B). The ground truth trajectory was estimated by batch optimization of the scan-to-map registration errors and IMU motion errors.

According to Fig. 11 and Table IV, the proposed method (Ours) outperforms all other approaches owing to online calibration and online uncertainty estimation. Although the first and second point cloud degeneration areas in Fig. 11 are shorter than the third one, FAST-LIO2 failed even in that first area. Even in changing terrain conditions, the proposed method was the most robust to all point cloud degeneration areas. Fig. 12 shows a time history of kinematic parameter K_i during this experiment. This result indicates that values of K_i are changed after around 140 seconds because the robot transited from bricks to outdoor stone tiles at this time. In addition, although the robot transited from outdoor stone

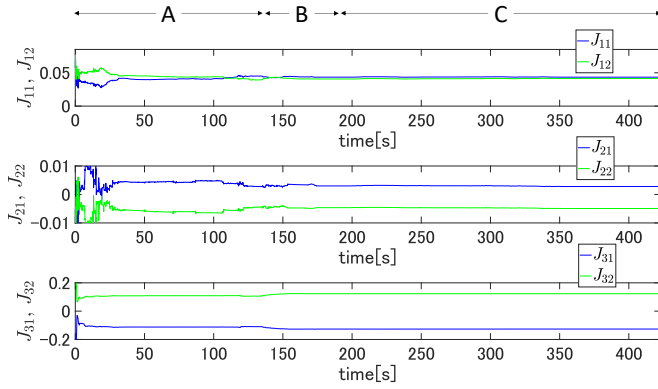


Fig. 12: Time histories of K_i . The process of transition environments is described as follows: A) bricks (0 to 140 seconds), B) outdoor stone tiles (140 to 190 seconds), C) indoor stone tiles (190 to 420 seconds).

tiles to indoor stone tiles after around 190 seconds, values of K_i are not changed. As shown in Fig. 10, the indoor stone's static friction coefficient is the almost same as the outdoor stone's value while these values differ from the blick's value. Hence, the result of Fig. 12 is reasonable. The reasonable adaptation of K_i to the different terrain conditions means the constant kinematic parameter factors worked properly. Therefore, we validated that the proposed online calibration enables robust odometry estimation even in changing terrain conditions.

V. CONCLUSION

This study presented a tightly-coupled LiDAR-IMU-wheel odometry algorithm with the online calibration of a kinematic model for skid-steering robots. In order to perform robust odometry estimation for point cloud degeneration, we proposed the full linear wheel odometry factor and derived its uncertainty. The first indoor experiment demonstrated that the proposed method is significantly robust to environments where point clouds degenerate while state-of-the-art LiDAR IMU odometry (FAST-LIO2) fails in these environments. In addition, the proposed method estimated the accurate sensor trajectory despite the existence of kinematic model errors (i.e., all-wheel radii are increased by 25%). The second outdoor experiment validated that the proposed method can accomplish an accurate odometry estimation in the grass owing to the uncertainty estimation. When the uncertainty estimation was included, the trajectory was twice as accurate compared to not including it. The third experiment showed that the kinematic parameters were estimated such as adapting to changes in terrain conditions and thus the proposed online calibration performs odometry estimation in robust to terrain conditions changes.

In future work, we plan to introduce a nonlinear term for a wheel odometry-based factor to validate a high-speed operation because this condition causes a nonlinear motion, such as wheel drift (sudden wheel slippage).

REFERENCES

[1] Z. Liu and F. Zhang, "Balm: Bundle adjustment for lidar mapping," *IEEE Robotics and Automation Letters*, vol. 6, no. 2, pp. 3184–3191, 2021.

[2] C. Qin, H. Ye, C. E. Pranata, J. Han, S. Zhang, and M. Liu, "Lins: A lidar-inertial state estimator for robust and efficient navigation," in *2020 IEEE International Conference on Robotics and Automation (ICRA)*. IEEE, 2020, pp. 8899–8906.

[3] W. Xu, Y. Cai, D. He, J. Lin, and F. Zhang, "Fast-lio2: Fast direct lidar-inertial odometry," *IEEE Transactions on Robotics*, vol. 38, no. 4, pp. 2053–2073, 2022.

[4] G. Anousaki and K. J. Kyriakopoulos, "A dead-reckoning scheme for skid-steered vehicles in outdoor environments," in *2004 IEEE International Conference on Robotics and Automation (ICRA)*. IEEE, 2004, pp. 580–585.

[5] A. Mandow, J. L. Martinez, J. Morales, J. L. Blanco, A. Garcia-Cerezo, and J. Gonzalez, "Experimental kinematics for wheeled skid-steer mobile robots," in *2007 IEEE/RSJ International Conference on Intelligent Robots and Systems (IROS)*. IEEE, 2007, pp. 1222–1227.

[6] T. Wang, Y. Wu, J. Liang, C. Han, J. Chen, and Q. Zhao, "Analysis and experimental kinematics of a skid-steering wheeled robot based on a laser scanner sensor," *Sensors*, vol. 15, no. 5, pp. 9681–9702, 2015.

[7] D. Baril, V. Grondin, S.-P. Deschênes, J. Laconte, M. Vaidis, V. Kubelka, A. Gallant, P. Giguere, and F. Pomerleau, "Evaluation of skid-steering kinematic models for subarctic environments," in *2020 17th Conference on Computer and Robot Vision (CRV)*. IEEE, 2020, pp. 198–205.

[8] R. Kümmerle, G. Grisetti, and W. Burgard, "Simultaneous calibration, localization, and mapping," in *2011 IEEE/RSJ International Conference on Intelligent Robots and Systems (IROS)*. IEEE, 2011, pp. 3716–3721.

[9] R. Kümmerle, G. Grisetti, and W. Burgard, "Simultaneous parameter calibration, localization, and mapping," *Advanced Robotics*, vol. 26, no. 17, pp. 2021–2041, 2012.

[10] W. Lee, K. Eickenhoff, Y. Yang, P. Geneva, and G. Huang, "Visual-inertial-wheel odometry with online calibration," in *2020 IEEE/RSJ International Conference on Intelligent Robots and Systems (IROS)*. IEEE, 2020, pp. 4559–4566.

[11] S. Bedín, J. Civera, and M. Nitsche, "Teach and repeat and wheel calibration for lidar-equipped omnidirectional drive robots," in *2023 European Conference on Mobile Robots (ECMR)*. IEEE, 2023, pp. 1–6.

[12] X. Zuo, M. Zhang, Y. Chen, Y. Liu, G. Huang, and M. Li, "Visual-inertial localization for skid-steering robots with kinematic constraints," in *The International Symposium of Robotics Research*. Springer, 2019, pp. 741–756.

[13] X. Zuo, M. Zhang, M. Wang, Y. Chen, G. Huang, Y. Liu, and M. Li, "Visual-based kinematics and pose estimation for skid-steering robots," *IEEE Transactions on Automation Science and Engineering*, 2022.

[14] K. Koide, M. Yokozuka, S. Oishi, and A. Banno, "Voxelized gicp for fast and accurate 3d point cloud registration," in *2021 IEEE International Conference on Robotics and Automation (ICRA)*. IEEE, 2021, pp. 11 054–11 059.

[15] M. Teschner, B. Heidelberg, M. Müller, D. Pomerantes, and M. H. Gross, "Optimized spatial hashing for collision detection of deformable objects," in *Vmv*, vol. 3, 2003, pp. 47–54.

[16] K. Koide, M. Yokozuka, S. Oishi, and A. Banno, "Globally consistent 3d lidar mapping with gpu-accelerated gicp matching cost factors," *IEEE Robotics and Automation Letters*, vol. 6, no. 4, pp. 8591–8598, 2021.

[17] —, "Globally consistent and tightly coupled 3d lidar inertial mapping," in *2022 International Conference on Robotics and Automation (ICRA)*. IEEE, 2022, pp. 5622–5628.

[18] C. Forster, L. Carlone, F. Dellaert, and D. Scaramuzza, "On-manifold preintegration for real-time visual-inertial odometry," *IEEE Transactions on Robotics*, vol. 33, no. 1, pp. 1–21, 2016.

[19] T. Qin, P. Li, and S. Shen, "Vins-mono: A robust and versatile monocular visual-inertial state estimator," *IEEE Transactions on Robotics*, vol. 34, no. 4, pp. 1004–1020, 2018.

[20] M. Kaess, H. Johannsson, R. Roberts, V. Ila, J. J. Leonard, and F. Dellaert, "isam2: Incremental smoothing and mapping using the bayes tree," *The International Journal of Robotics Research*, vol. 31, no. 2, pp. 216–235, 2012.

[21] Z. Zhang and D. Scaramuzza, "A tutorial on quantitative trajectory evaluation for visual (-inertial) odometry," in *2018 IEEE/RSJ International Conference on Intelligent Robots and Systems (IROS)*. IEEE, 2018, pp. 7244–7251.